

**Antiparallel spin polarization and spin current
induced by thermal current and locally-broken inversion symmetry
in a double-quantum-well structure**

Yuta Suzuki^{*,1,2}(Yuuta.Suzuki@yokogawa.com)

Yuma Kitagawa^{1,2} Shin-ichiro Tezuka² and Hiroshi Akera³

¹*Division of Applied Physics, Graduate School of Engineering,
Hokkaido University, Sapporo, Hokkaido, 060-8628, Japan*

²*Sensing Research & Development Department,*

*Innovation Center, Marketing Headquarters,
Yokogawa Electric Corporation, Tokyo, 180-8750, Japan*

³*Division of Applied Physics, Faculty of Engineering,
Hokkaido University, Sapporo, Hokkaido, 060-8628, Japan*

(Dated: December 14, 2023)

Abstract

Generating a nonequilibrium spin polarization with a driving force has been first realized by the electric current in a system with broken inversion symmetry and extended to that induced by the thermal current and that appearing in an inversion-symmetric system with locally-broken inversion symmetry. This paper theoretically explores the spin polarization generated by the thermal current and the locally-broken inversion symmetry in a symmetric double-quantum-well structure (DQWS). This thermally-induced spin polarization (TISP) appears in the antiparallel configuration with the TISP of two wells in opposite directions. The calculation using the Boltzmann equation in the relaxation-time approximation under the condition of zero charge current shows that the local TISP exhibits the maximum at a finite Rashba spin-orbit interaction when the electron density is fixed. This is because the local TISP in the DQWS is enhanced at the chemical potential near the bottom of the first-excited subband. This enhancement also occurs in a single quantum well with globally-broken inversion symmetry. Another finding is that the maximum of the local TISP appears at a nonzero interwell coupling. The spin current by the diffusion of the local TISP into an adjacent electrode is also calculated.

I. INTRODUCTION

Current-induced spin polarization (CISP) [1–6] is generated by breaking the time-reversal symmetry with current in a system with broken inversion symmetry through the action of the spin-orbit interaction (SOI). The CISP on surfaces of topological insulators [7–9] and in two-dimensional electron systems (2DES) [10–14] has been demonstrated to create the spin diffusion current which can be used for switching the magnetization in ferromagnetic memory.

Thermally-induced spin polarization (TISP) has also been studied theoretically [15–19] in the 2DES with the Rashba SOI [20–23]. In the TISP the time-reversal symmetry is broken by the thermal current, which is the flow of electronic excitations from a lower to a higher eigenstate. Therefore the TISP is large when the difference between spin polarizations of the two eigenstates is large and signs of differences are the same for all excitations. We expect that such requirements can be met by adjusting system parameters.

Locally-broken inversion symmetry in a system with the global inversion symmetry [24–39] has also been used to create the CISP in the antiparallel configuration. Such antiparallel CISP is a nonequilibrium analog of the equilibrium antiferromagnetism. Consider an inversion-symmetric system consisting of two sublattices or two layers. If the inversion symmetry in each sublattice (each layer) is broken to produce a local effective magnetic field acting on spin, the sum of the spin density over a pair of spin-degenerate eigenstates is locally nonzero [25], although it vanishes globally when integrated over the two sublattices (layers). By breaking the time reversal symmetry, this antiparallel spin density gives rise to the antiparallel CISP [24, 26, 37–39]. This antiparallel CISP has been demonstrated to reverse the sublattice magnetization of antiferromagnet [28, 34] in antiferromagnetic memory [40]. The antiparallel CISP can also be used to generate the spin current by a selective coupling of an electrode to one sublattice (layer) as theoretically demonstrated in a double-quantum-well structure (DQWS) [37] and in a buckled atomic layer [38]. The magnitude of the spin current has been shown to be comparable to that generated by globally-broken inversion symmetry [37, 38].

Table. I. Current-induced spin polarization and thermally-induced spin polarization.

inversion symmetry	globally broken	locally broken
CISP	Refs.[1–6]	Refs.[24, 26, 37–39]
TISP	Refs.[15–19]	this study

In this study we employ both the thermal current and the locally-broken inversion symmetry to produce the spin polarization (Table. I shows the position of this study in the field). We choose the DQWS [41–49] as the simplest system with the locally-broken inversion symmetry. In the DQWS, which is symmetric with respect to the plane between two wells, the Rashba SOI gives the antiparallel effective magnetic field. We calculate the thermally-induced antiparallel spin polarization (antiparallel TISP) by using the Boltzmann equation in the relaxation-time approximation under the condition of zero charge current. We plot the local TISP (l -TISP) in one well as a function of the strength of the Rashba SOI and that of the interwell coupling with an aim to search optimum values of these system parameters which maximize the magnitude of the l -TISP. We find that the l -TISP exhibits

the maximum at a finite Rashba SOI and a nonzero interwell coupling when the electron density is fixed.

The organization of this paper is as follows. Section II A presents a general scheme for generating the spin current using the l -TISP in a system with the locally-broken inversion symmetry. Section II B describes the Hamiltonian of the DQWS and that of the electrode with their eigenstates. In Section III we employ the Boltzmann equation in the relaxation-time approximation to derive the distribution function of the DQWS with in-plane gradients of the temperature and the electrochemical potential. Section IV presents calculated results of the l -TISP under the condition of zero charge current. In addition this section derives the formula for the spin current flowing to the electrode, by introducing the Hamiltonian describing the tunneling between the DQWS and the electrode, and shows that the spin current is proportional to the l -TISP under an assumption presented there with respect to the electron tunneling. Conclusions are given in Section V.

II. MODEL AND HAMILTONIAN

A. General Model

Figure 1(a) presents a general model for the thermal generation of the spin current from a system with the inversion symmetry, while Figure 1(b) and (c) show two example systems, the DQWS and the group-IV atomic layer, respectively. The temperature difference between reservoir 1 and 2, $T_1 - T_2$ (> 0), is introduced to produce the electron-temperature gradient ∇T_e , which thermally induces the antiparallel spin polarization in A and B [layers L and R in Figure 1(b) and sublattices A and B in Figure 1(c)]. This thermally-induced local spin polarization (l -TISP) in each of A and B is then selectively extracted into electrodes A and B, respectively. We impose the condition of the vanishing charge current [50], which produces the electrochemical-potential gradient $\nabla \mu_{ec}$. We describe the eigenstate of the l -TISP generator as $|\nu \mathbf{k}\rangle$ with the wave vector $\mathbf{k} = (k_x, k_y)$ and the band index ν . In the electrodes we neglect the SOI and choose the eigenstate to be the eigenvector of $\hat{\sigma}_y$ the y component of the Pauli spin operator, which satisfies $\hat{\sigma}_y |\sigma_y\rangle = \sigma_y |\sigma_y\rangle$ with $\sigma_y = \pm 1$. Here

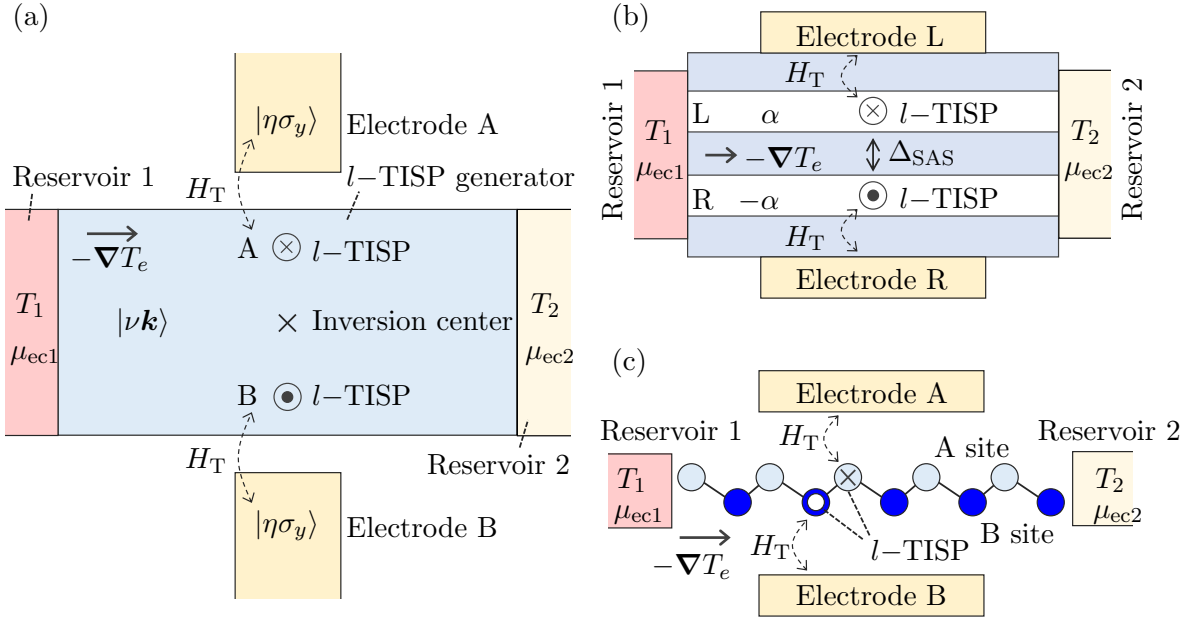


Figure 1. (a) General model for the generation of the spin current by l -TISP. (b) DQWS model. (c) Atomic-layer model.

we take the y axis in the direction of the l -TISP. Then the eigenstate of the electrode is expressed as $|\xi\eta\sigma_y\rangle$, where $\xi = A, B$ and η represents other quantum numbers.

We describe the coupling between the l -TISP generator and each electrode by the tunneling Hamiltonian H_T . Then the Hamiltonian of our general model in Figure 1(a) is expressed by

$$H = H_0 + H_{El} + H_T, \quad (1)$$

where H_0 and H_{El} are the Hamiltonian of the l -TISP generator and that of the electrodes, respectively. Their eigenvectors satisfy

$$H_0 |\nu\mathbf{k}\rangle = \varepsilon_{\nu\mathbf{k}} |\nu\mathbf{k}\rangle, \quad H_{El} |\xi\eta\sigma_y\rangle = \varepsilon_\eta |\xi\eta\sigma_y\rangle, \quad \xi = A, B \quad (2)$$

where $\varepsilon_{\nu\mathbf{k}}$ and ε_η are the corresponding eigenvalues.

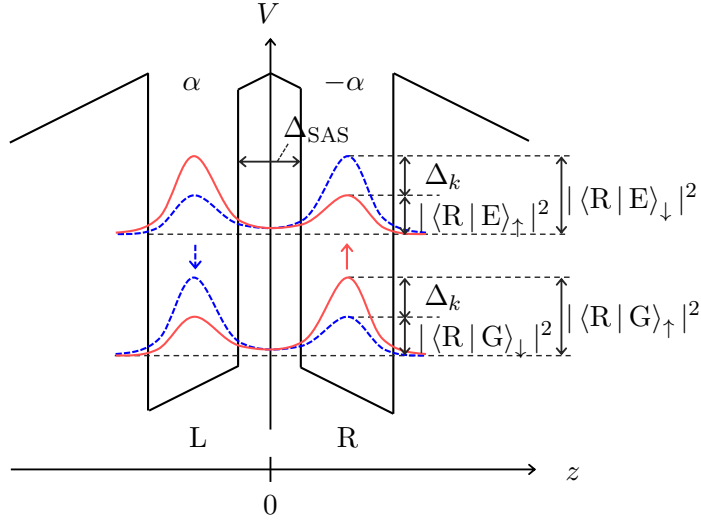


Figure 2. Potential V and the local spin density in each eigenstate of the DQWS [Figure 1(b)]. Red solid and blue dashed lines represent the schematic distribution of spin-up and spin-down states, respectively, with wave number k in the ground subband G and the first excited subband E. The direction of spin is parallel or antiparallel to the effective magnetic field. Δ_k is the magnitude of the local spin polarization in each well.

B. DQWS as the simplest example

We study the l -TISP in the DQWS, as the simplest example of inversion-symmetric structure, in the following. The DQWS [Figure 1(b)] consists of two wells, L and R, with the Rashba spin-orbit coefficients, $\alpha (> 0)$ and $-\alpha$, respectively. The strength of the coupling between L and R wells is denoted by Δ_{SAS} . Wells L and R are selectively coupled to electrodes L and R, respectively.

The Hamiltonian of the DQWS, with the potential shown in Figure 2, is given by

$$H_0 = \frac{\hat{p}_x^2 + \hat{p}_y^2}{2m} + H_{\perp}, \quad (3)$$

where \hat{p}_x and \hat{p}_y are the momentum operators and m is the effective mass of the conduction band. The second term H_{\perp} , for the motion perpendicular to the DQWS, is given by

$$H_{\perp} = -\frac{1}{2}\Delta_{\text{SAS}}\hat{\tau}_1 + \frac{\alpha}{\hbar}\hat{\tau}_3(\hat{p}_y\hat{\sigma}_x - \hat{p}_x\hat{\sigma}_y), \quad (4)$$

where the first term represents the interwell coupling and the second term expresses the antiparallel Rashba effective magnetic field. Here $\hat{\tau}_\gamma$ ($\gamma = 1, 2$ and 3) is the Pauli operator for pseudospin [39, 51, 52] defined by

$$\hat{\tau}_1 = |\mathbf{R}\rangle \langle \mathbf{L}| + |\mathbf{L}\rangle \langle \mathbf{R}|, \quad (5)$$

$$\hat{\tau}_2 = i |\mathbf{R}\rangle \langle \mathbf{L}| - i |\mathbf{L}\rangle \langle \mathbf{R}|, \quad (6)$$

$$\hat{\tau}_3 = |\mathbf{L}\rangle \langle \mathbf{L}| - |\mathbf{R}\rangle \langle \mathbf{R}|, \quad (7)$$

where $|\mathbf{L}\rangle$ and $|\mathbf{R}\rangle$ represent the lowest bound state in the left and right wells, respectively.

The eigenvector is given by $|n\sigma\mathbf{k}\rangle = |n\rangle|\sigma\rangle|\mathbf{k}\rangle$. Here $|\mathbf{k}\rangle$ is the eigenvector of $\hat{\mathbf{p}} = (\hat{p}_x, \hat{p}_y)$ corresponding to the eigenvalue $\hbar\mathbf{k}$. For each \mathbf{k} , $|\sigma\rangle$ is defined by $\mathbf{e}_b \cdot \hat{\boldsymbol{\sigma}} |\sigma\rangle = \sigma |\sigma\rangle$ where $\mathbf{e}_b = k^{-1}(k_y, -k_x, 0)$ with $k = \sqrt{k_x^2 + k_y^2}$ which is the unit vector in the direction of the effective magnetic field, $\hat{\boldsymbol{\sigma}} = (\hat{\sigma}_x, \hat{\sigma}_y, \hat{\sigma}_z)$, and $\sigma = \pm 1$. The vector $|n\rangle$ ($n = \pm 1$) is given, for each k and each σ , by

$$|n\rangle = \frac{1}{\sqrt{2}} \left(\sqrt{1 + n\sigma\Delta_k} |\mathbf{L}\rangle - n\sqrt{1 - n\sigma\Delta_k} |\mathbf{R}\rangle \right), \quad (8)$$

$$\Delta_k = 2\alpha k / \sqrt{\Delta_{\text{SAS}}^2 + (2\alpha k)^2}. \quad (9)$$

We also use $n = \text{G}$ for $n = -1$ and $n = \text{E}$ for $n = 1$, since they are the ground state and the first excited state, respectively. The local spin polarization in each well of state $|n\rangle$ at \mathbf{k} becomes

$$\sum_{\sigma} \langle n\sigma\mathbf{k} | \hat{\boldsymbol{\sigma}} P_{\xi} | n\sigma\mathbf{k} \rangle = \xi n \Delta_k \mathbf{e}_b, \quad (10)$$

where $P_{\xi} = |\xi\rangle\langle\xi|$ is the projection operator onto well ξ ($\xi = \text{L}, \text{R}$) with $\xi = 1$ for $\xi = \text{L}$ and $\xi = -1$ for $\xi = \text{R}$. Equation (10) shows that the magnitude of the local spin polarization is Δ_k , and its direction is opposite between $\xi = \text{L}$ and R and between $n = \text{G}$ and E as shown in Figure 2.

The eigenvalue of H_0 is given by

$$\varepsilon_{nk} = \frac{\hbar^2 k^2}{2m} + \frac{n}{2} \sqrt{\Delta_{\text{SAS}}^2 + (2\alpha k)^2}, \quad (11)$$

The eigenvalue has no dependence on σ because the DQWS has the inversion symmetry.

The Hamiltonian of electrode ξ ($=$ L, R) is assumed to be

$$H_{\text{El}} = \frac{\hat{p}_x^2 + \hat{p}_y^2 + \hat{p}_z^2}{2m_{\text{El}}} + \varepsilon_0. \quad (12)$$

Here the effective mass m_{El} is the same in $\xi =$ L and R, and $\varepsilon_0 (< 0)$ is the energy at the band bottom. The eigenvector is $|\xi \mathbf{k} k_z \sigma_y\rangle$ and the eigenenergy is

$$\varepsilon_{k k_z} = \frac{\hbar^2(k^2 + k_z^2)}{2m_{\text{El}}} + \varepsilon_0. \quad (13)$$

III. BOLTZMANN EQUATION AND DISTRIBUTION FUNCTION

We calculate the l -TISP, the spin current, and the inplane charge current of the DQWS model in Sec. II B by employing the Boltzmann equation in the first order of ∇T_e and $\nabla \mu_{\text{ec}} = \nabla \mu + e\mathbf{E}$ where μ is the chemical potential, $e (> 0)$ is the absolute value of the electronic charge, and \mathbf{E} is the inplane electric field. The distribution function $f_{n\mathbf{k}}$ with n the band index and \mathbf{k} the inplane wave vector is decomposed into the equilibrium distribution function for local values of $\mu(\mathbf{r})$ and $T_e(\mathbf{r})$ with $\mathbf{r} = (x, y)$ and the deviation $f_{n\mathbf{k}}^{(1)}$ in the first order of ∇T_e and $\nabla \mu_{\text{ec}}$:

$$f_{n\mathbf{k}} = f^{(0)}(\varepsilon_{n\mathbf{k}}, \mu(\mathbf{r}), T_e(\mathbf{r})) + f_{n\mathbf{k}}^{(1)}, \quad (14)$$

where $f^{(0)}(\varepsilon, \mu, T_e) = \{\exp[(\varepsilon - \mu)/k_B T_e] + 1\}^{-1}$ with k_B the Boltzmann constant. The steady-state Boltzmann equation for $f_{n\mathbf{k}}$ is given, in the relaxation time approximation with the momentum relaxation time τ_p , by

$$\mathbf{v}_{n\mathbf{k}} \cdot \frac{\partial f_{n\mathbf{k}}}{\partial \mathbf{r}} + \frac{(-e)\mathbf{E}}{\hbar} \cdot \frac{\partial f_{n\mathbf{k}}}{\partial \mathbf{k}} = -\frac{f_{n\mathbf{k}}^{(1)}}{\tau_p}, \quad (15)$$

where $\mathbf{v}_{n\mathbf{k}} = \hbar^{-1} \frac{\partial \varepsilon_{n\mathbf{k}}}{\partial \mathbf{k}}$. From Eq.(15), $f_{n\mathbf{k}}^{(1)}$ is obtained as [50]

$$f_{n\mathbf{k}}^{(1)} = \frac{\tau_p}{\hbar} \frac{\partial f^{(0)}}{\partial \mathbf{k}} \cdot \left(\nabla \mu_{\text{ec}} + \frac{\varepsilon_{n\mathbf{k}} - \mu}{T_e} \nabla T_e \right). \quad (16)$$

IV. CALCULATED RESULTS

A. Antiparallel TISP

The l -TISP in well ξ of the DQWS per unit area, $\boldsymbol{\sigma}_\xi = (\sigma_{x\xi}, \sigma_{y\xi}, \sigma_{z\xi})$, is given, using the first-order deviation $f_{n\mathbf{k}}^{(1)}$, by

$$\boldsymbol{\sigma}_\xi = \frac{1}{S} \sum_{n\sigma\mathbf{k}} f_{n\mathbf{k}}^{(1)} \langle n\sigma\mathbf{k} | \hat{\boldsymbol{\sigma}} P_\xi | n\sigma\mathbf{k} \rangle, \quad (17)$$

with S the system area. Gradients $\nabla\mu_{ec}$ and ∇T_e in $f_{n\mathbf{k}}^{(1)}$ [Eq.(16)] are related by vanishing the charge current density, \mathbf{j}^c , which is given by

$$\mathbf{j}^c = -\frac{e}{S} \sum_{n\sigma\mathbf{k}} f_{n\mathbf{k}}^{(1)} \mathbf{v}_{n\mathbf{k}} = L^{\mu_{ec}} \nabla\mu_{ec} + L^{T_e} \nabla T_e, \quad (18)$$

$$L^{\mu_{ec}} = \sum_n L_n^{\mu_{ec}}, \quad L_n^{\mu_{ec}} = \frac{2e\tau_p}{S\hbar} \sum_{\mathbf{k}} \left(\frac{k_x}{k}\right)^2 \left(-\frac{\partial f^{(0)}}{\partial k}\right) v_{n\mathbf{k}}, \quad (19)$$

$$L^{T_e} = \sum_n L_n^{T_e}, \quad L_n^{T_e} = \frac{2e\tau_p}{S\hbar} \sum_{\mathbf{k}} \left(\frac{k_x}{k}\right)^2 \left(-\frac{\partial f^{(0)}}{\partial k}\right) \frac{\varepsilon_{n\mathbf{k}} - \mu}{T_e} v_{n\mathbf{k}}, \quad (20)$$

where the dependence of τ_p on n and k is neglected, and $v_{n\mathbf{k}} = |\mathbf{v}_{n\mathbf{k}}|$. From $\mathbf{j}^c = 0$, we obtain $\nabla\mu_{ec} = -(L^{T_e}/L^{\mu_{ec}})\nabla T_e$. We choose the x axis in the direction of the temperature gradient, $\nabla T_e = (\nabla_x T_e, 0)$. Then the l -TISP appears in the y direction and $\sigma_{y\xi}$ is given by

$$\sigma_{y\xi} = \xi(\sigma^{\mu_{ec}} \nabla_x \mu_{ec} + \sigma^{T_e} \nabla_x T_e) = \xi \left(-\sigma^{\mu_{ec}} \frac{L^{T_e}}{L^{\mu_{ec}}} + \sigma^{T_e} \right) \nabla_x T_e, \quad (21)$$

$$\sigma^{\mu_{ec}} = \sum_n \sigma_n^{\mu_{ec}}, \quad \sigma_n^{\mu_{ec}} = \frac{n\tau_p}{S\hbar} \sum_{\mathbf{k}} \left(\frac{k_x}{k}\right)^2 \left(-\frac{\partial f^{(0)}}{\partial k}\right) \Delta_{\mathbf{k}}, \quad (22)$$

$$\sigma^{T_e} = \sum_n \sigma_n^{T_e}, \quad \sigma_n^{T_e} = \frac{n\tau_p}{S\hbar} \sum_{\mathbf{k}} \left(\frac{k_x}{k}\right)^2 \left(-\frac{\partial f^{(0)}}{\partial k}\right) \frac{\varepsilon_{n\mathbf{k}} - \mu}{T_e} \Delta_{\mathbf{k}}. \quad (23)$$

The l -TISPs in well L and R are in opposite direction, $\sigma_{yL} = -\sigma_{yR}$, and the contributions from subband G and E are also in opposite direction, $\sigma_G^{\mu_{ec}} = -\sigma_E^{\mu_{ec}}$ and $\sigma_G^{T_e} = -\sigma_E^{T_e}$.

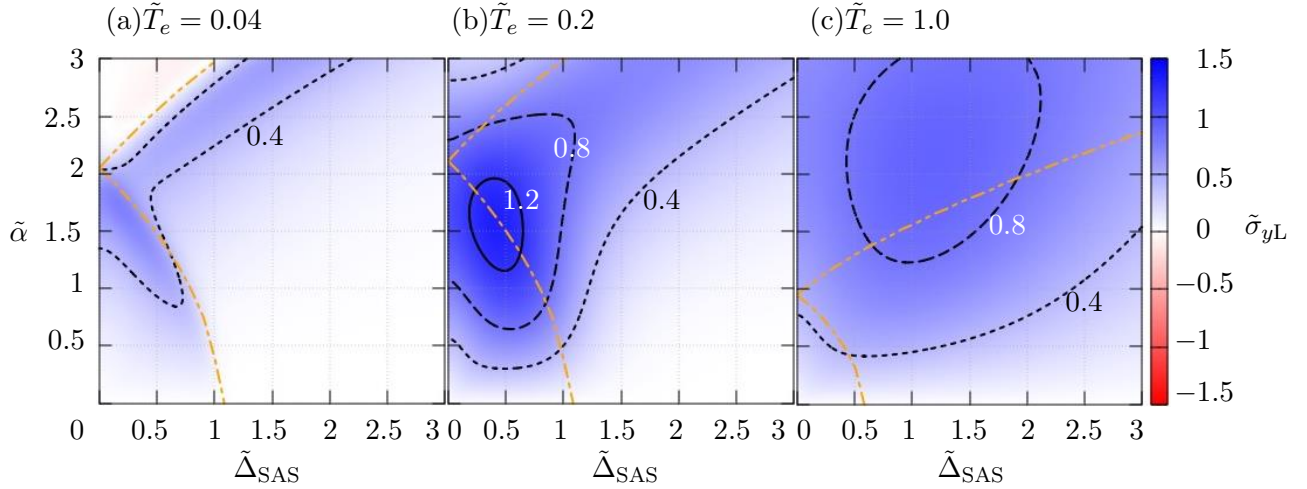


Figure 3. The l -TISP σ_{yL} as functions of the temperature $k_B T_e$, the interwell-coupling strength Δ_{SAS} , and the Rashba-SOI intensity α . Dimensionless parameters are introduced as $\tilde{\sigma}_{yL} = \sigma_{yL}/[\tau_p k_{F0}/(4\pi\hbar)\nabla_x(k_B T_e)]$, $\tilde{T}_e = k_B T_e/\varepsilon_{F0}$, $\tilde{\Delta}_{\text{SAS}} = \Delta_{\text{SAS}}/\varepsilon_{F0}$, and $\tilde{\alpha} = 2\alpha k_{F0}/\varepsilon_{F0}$. ε_{F0} and k_{F0} are the Fermi energy and the Fermi wave number at $\Delta_{\text{SAS}} = \alpha = T_e = 0$. On the orange dashed-dotted (dashed double-dotted) line, the chemical potential coincides with the energy at $\mathbf{k} = 0$ of the first excited subband E (the ground subband G).

Figure 3 presents dependences of σ_{yL} on the strength of the Rashba SOI (α) and that of the interwell coupling (Δ_{SAS}). In this calculation, we determine the chemical potential μ so that the electron number density

$$N_e = \frac{1}{S} \sum_{n\sigma\mathbf{k}} f_{n\mathbf{k}} \quad (24)$$

is a constant. Then μ depends on values of α , Δ_{SAS} , and T_e . Figure 3(a)–(c) show plots at different temperatures, $\tilde{T}_e = k_B T_e/\varepsilon_{F0} = 0.04, 0.2$, and 1.0 , respectively, where ε_{F0} is the Fermi energy at $\Delta_{\text{SAS}} = \alpha = T_e = 0$. The l -TISP approaches zero at $T_e \rightarrow 0$ and at $T_e \rightarrow \infty$. Our calculation shows that the largest value of σ_{yL} appears around $\tilde{T}_e \sim 0.2$. The orange dashed-dotted and dashed double-dotted lines correspond to the chemical potential coinciding with the energy at $\mathbf{k} = 0$ of the first excited subband E and that of the ground subband G, respectively (the bottom of the first excited subband is at $\mathbf{k} = 0$ for any values of Δ_{SAS} , while that of the ground subband is at $\mathbf{k} = 0$ for $\Delta_{\text{SAS}} \geq 2\alpha k_{\text{SO}}$ with $k_{\text{SO}} = m\alpha/\hbar^2$). We have found

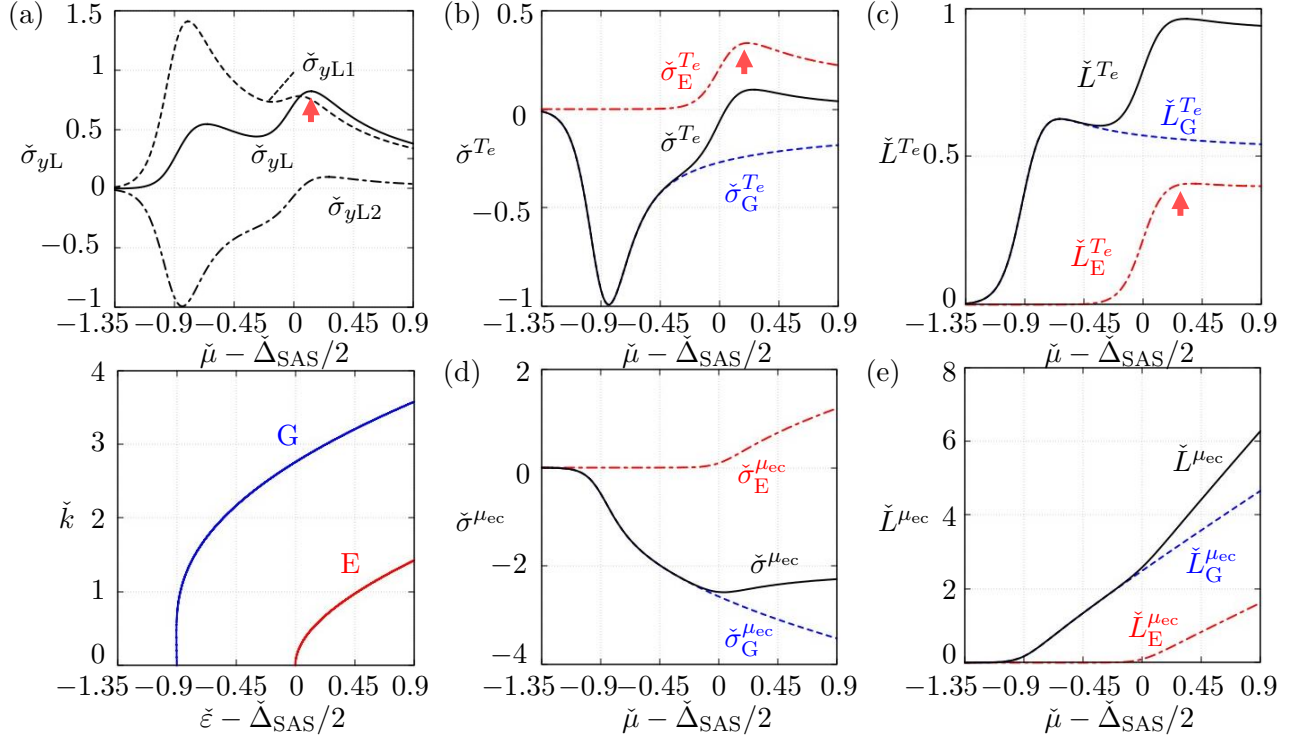


Figure 4. (a) The l -TISP σ_{yL} and its decomposition into the first term $\sigma_{yL1} = (-\sigma^{\mu_{ec}} L^{T_e} / L^{\mu_{ec}}) \nabla_x T_e$ and the second term $\sigma_{yL2} = \sigma^{T_e} \nabla_x T_e$ as a function of the chemical potential μ . Dimensionless values are defined by $\check{\sigma}_{yL} = \sigma_{yL} / \sigma_0$, $\check{\sigma}_{yL1} = \sigma_{yL1} / \sigma_0$, $\check{\sigma}_{yL2} = \sigma_{yL2} / \sigma_0$, and $\check{\mu} = \mu / (2\alpha k_{SO})$ with $\sigma_0 = \tau_p k_{SO} / (4\pi\hbar) \nabla_x (k_B T_e)$ and $k_{SO} = m\alpha / \hbar^2$. Δ_{SAS} and $k_B T_e$ are fixed at $\check{\Delta}_{SAS} = \Delta_{SAS} / (2\alpha k_{SO}) = 0.9$ and $\check{T}_e = k_B T_e / (2\alpha k_{SO}) = 0.07$. In the μ sweep, values of $\check{\Delta}_{SAS}$ and \check{T}_e do not change, while those of $\tilde{\Delta}_{SAS}$ and \tilde{T}_e (Figure 3) change. The red arrow indicates the peak location of the l -TISP around the bottom of the first excited subband. The lower plot shows the ground (G) and the first excited (E) subbands with $\check{k} = k / k_{SO}$. (b)–(e) Coefficients σ^{T_e} , L^{T_e} , $\sigma^{\mu_{ec}}$, and $L^{\mu_{ec}}$, with their decompositions into the ground subband G and the first excited subband E, as a function of the chemical potential. $\check{\sigma}^{\mu_{ec}} = \sigma^{\mu_{ec}} / \sigma_\alpha$ and $\check{\sigma}^{T_e} = \sigma^{T_e} / (\sigma_\alpha k_B)$ with $\sigma_\alpha = \tau_p k_{SO} / (4\pi\hbar)$, while $\check{L}^{\mu_{ec}} = L^{\mu_{ec}} / L_\alpha$ and $\check{L}^{T_e} = L^{T_e} / (L_\alpha k_B)$ with $L_\alpha = e\tau_p \alpha k_{SO} / (\pi\hbar^2)$.

that larger values of the l -TISP appear in the vicinity of these lines. This enhancement is most clearly seen in the panel of $\tilde{T}_e = 0.04$ and remains at a higher temperature of $\tilde{T}_e = 0.2$.

To closely investigate the above-mentioned enhancement around the orange lines [Figure 3], in Figure 4(a) we plot σ_{yL} as a function of the chemical potential μ at $(\check{\Delta}_{SAS}, \check{T}_e) =$

(0.9, 0.07) where $\tilde{\Delta}_{\text{SAS}} = \Delta_{\text{SAS}}/(2\alpha k_{\text{SO}})$ and $\tilde{T}_e = k_{\text{B}}T_e/(2\alpha k_{\text{SO}})$. The l -TISP σ_{yL} exhibits two peaks with changing μ , one near the first excited subband bottom and the other near the ground subband bottom (the ground subband bottom is at $\mathbf{k} = 0$ when $\tilde{\Delta}_{\text{SAS}} \geq 1$). Figure 4(a) also shows that the first term $(-\sigma^{\mu ec} L^{T_e}/L^{\mu ec})\nabla_x T_e$ in Eq.(21), which appears by imposing the zero-charge-current condition, is comparable in magnitude to the second term $\sigma^{T_e}\nabla_x T_e$. Signs of these two terms are opposite (same) in the vicinity of the ground (first excited) subband bottom. This is why the peak of σ_{yL} near the first excited subband bottom is higher. To find out the origin of the peaks in σ_{yL} , we separately plot σ^{T_e} , $\sigma^{\mu ec}$, L^{T_e} , and $L^{\mu ec}$ in Figure 4(b)–(e). Then we find that σ^{T_e} and L^{T_e} with the factor $(\varepsilon_{nk} - \mu)$ in their expressions, Eqs.(23) and (20), exhibit larger variations around subband bottoms (leading to the peaks) compared to $\sigma^{\mu ec}$ and $L^{\mu ec}$. Figure 4(b)–(e) also decompose each of σ^{T_e} , $\sigma^{\mu ec}$, L^{T_e} , and $L^{\mu ec}$ into contributions from two subbands, confirming that the contribution of each subband shows a large variation around its bottom. Since $\sigma^{\mu ec}$ represents the local CISP, our calculation shows that the l -TISP exhibits larger variations with the chemical potential in comparison to the local CISP.

Now we focus on the higher peak of σ_{yL} around the first excited subband bottom at $\varepsilon = \Delta_{\text{SAS}}/2$, which mainly comes from the peak of $\sigma_{\text{E}}^{T_e}$ and that of $L_{\text{E}}^{T_e}$. In Figure 5(a) $\sigma_{\text{E}}^{T_e}$ is divided into the contribution from electron excitations ($\varepsilon - \mu \geq 0$), $\sigma_{\text{Ee}}^{T_e}$, and that from hole excitations ($\varepsilon - \mu < 0$), $\sigma_{\text{Eh}}^{T_e}$:

$$\sigma_{\text{E}}^{T_e} = \sigma_{\text{Ee}}^{T_e} + \sigma_{\text{Eh}}^{T_e} \quad (25)$$

$$\sigma_{\text{Ee}}^{T_e} = \frac{\tau_p}{4\pi\hbar} \int_{\frac{\Delta_{\text{SAS}}}{2}}^{\infty} d\varepsilon \theta(\varepsilon - \mu) g(\varepsilon) \left(-\frac{\partial f^{(0)}}{\partial \varepsilon} \right) \frac{\varepsilon - \mu}{T_e}, \quad (26)$$

$$\sigma_{\text{Eh}}^{T_e} = \frac{\tau_p}{4\pi\hbar} \int_{\frac{\Delta_{\text{SAS}}}{2}}^{\infty} d\varepsilon \theta(-\varepsilon + \mu) g(\varepsilon) \left(-\frac{\partial f^{(0)}}{\partial \varepsilon} \right) \frac{\varepsilon - \mu}{T_e} \quad (27)$$

where $g(\varepsilon) = k\Delta_k$ with k determined by $\varepsilon = \varepsilon_{nk}$ [Equation (11)] and $\theta(\varepsilon)$ is defined by $\theta(\varepsilon) = 1$ ($\varepsilon \geq 0$) and $\theta(\varepsilon) = 0$ ($\varepsilon < 0$). In the chemical-potential region below the subband bottom ($\mu < \Delta_{\text{SAS}}/2$) the hole contribution $\sigma_{\text{Eh}}^{T_e}$ is absent and the positive electron contribution $\sigma_{\text{Ee}}^{T_e}$ increases with increasing the chemical potential. On the other hand, in the region of $\mu \geq \Delta_{\text{SAS}}/2$, the negative hole contribution $\sigma_{\text{Eh}}^{T_e}$ starts to suppress $\sigma_{\text{E}}^{T_e}$ which eventually

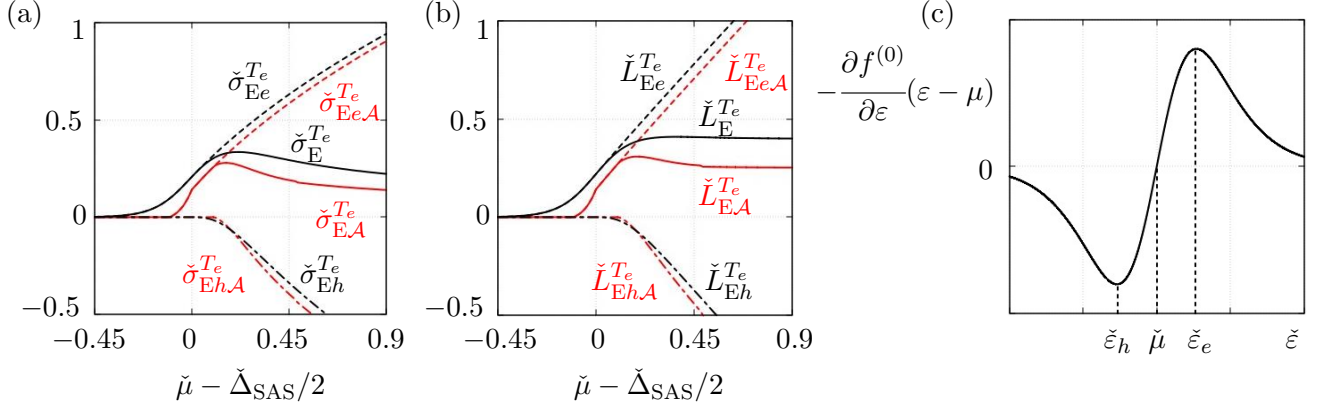


Figure 5. (a) The decomposition of $\check{\sigma}_{\text{E}e}^{T_e}$ at $(\check{\Delta}_{\text{SAS}}, \check{T}_e) = (0.9, 0.07)$ in Figure 4(b) into the contribution from electron excitations ($\varepsilon - \mu \geq 0$), $\sigma_{\text{E}e}^{T_e}$ [Equation (26)], and that from hole excitations ($\varepsilon - \mu < 0$), $\sigma_{\text{E}h}^{T_e}$ [Equation (27)]. Also plotted are approximate analytical expressions, $\check{\sigma}_{\text{E}e\text{A}}^{T_e}$ [Equation (31)] and $\check{\sigma}_{\text{E}h\text{A}}^{T_e}$ [Equation (32)], with $\check{\sigma}_{\text{E}e\text{A}}^{T_e} = \check{\sigma}_{\text{E}e}^{T_e} + \check{\sigma}_{\text{E}h\text{A}}^{T_e}$. (b) The same decomposition of $\check{L}_{\text{E}}^{T_e}$ in Figure 4(c). (c) The energy dependence of $[-\partial f^{(0)}/\partial \varepsilon](\varepsilon - \mu)$ in expressions of $\sigma_{\text{E}e}^{T_e}$ and $\sigma_{\text{E}h}^{T_e}$ [Equations (26) and (27)]. The maximum and the minimum are located around $\check{\varepsilon}_e = \check{\mu} + 1.5\check{T}_e$ and $\check{\varepsilon}_h = \check{\mu} - 1.5\check{T}_e$, respectively.

decreases with increasing μ . Thus the peak of $\sigma_{\text{E}e}^{T_e}$ appears near the subband bottom.

The same explanation holds for the peak of $L_{\text{E}}^{T_e}$. Figure 5(b) presents chemical-potential dependences of its electron and hole contributions, $L_{\text{E}e}^{T_e}$ and $L_{\text{E}h}^{T_e}$, given by

$$L_{\text{E}}^{T_e} = L_{\text{E}e}^{T_e} + L_{\text{E}h}^{T_e}, \quad (28)$$

$$L_{\text{E}e}^{T_e} = \frac{e\tau_p}{2\pi\hbar} \int_{\frac{\Delta_{\text{SAS}}}{2}}^{\infty} d\varepsilon \theta(\varepsilon - \mu) h(\varepsilon) \left(-\frac{\partial f^{(0)}}{\partial \varepsilon} \right) \frac{\varepsilon - \mu}{T_e}, \quad (29)$$

$$L_{\text{E}h}^{T_e} = \frac{e\tau_p}{2\pi\hbar} \int_{\frac{\Delta_{\text{SAS}}}{2}}^{\infty} d\varepsilon \theta(-\varepsilon + \mu) h(\varepsilon) \left(-\frac{\partial f^{(0)}}{\partial \varepsilon} \right) \frac{\varepsilon - \mu}{T_e}, \quad (30)$$

where $h(\varepsilon) = kv_{\text{E}k}$. Therefore the change in the balance between electron and hole contributions in $\sigma_{\text{E}e}^{T_e}$ and $L_{\text{E}}^{T_e}$ is responsible for the formation of their peaks, leading to the peak formation in the l -TISP σ_{yL} .

Finally we consider the reason why the maximum of l -TISP σ_{yL} appears at a non-zero

interwell coupling Δ_{SAS} in Figure 3 by estimating the Δ_{SAS} dependence of the peak height in each of $\sigma_{\text{E}}^{T_e}$ and $L_{\text{E}}^{T_e}$ with use of their approximate analytical expressions. The approximation is made by replacing $g(\varepsilon)$ in Eq. (26) [Eq. (27)] by its value at $\varepsilon_e = \mu + 1.5k_{\text{B}}T_e$ [$\varepsilon_h = \mu - 1.5k_{\text{B}}T_e$] because at $\varepsilon = \varepsilon_e$ [$\varepsilon = \varepsilon_h$] the absolute value of $[-\partial f^{(0)}/\partial \varepsilon]$ ($\varepsilon - \mu$) in Eq. (26) [Eq. (27)] is nearly the largest in $\varepsilon > \mu$ [$\varepsilon < \mu$] as shown in Figure 5(c). Then the approximate expressions become

$$\sigma_{\text{E}e\text{A}}^{T_e} = \frac{\tau_p}{4\pi\hbar}g(\mu + 1.5k_{\text{B}}T_e) \int_{\frac{\Delta_{\text{SAS}}}{2}}^{\infty} d\varepsilon \theta(\varepsilon - \mu) \left(-\frac{\partial f^{(0)}}{\partial \varepsilon} \right) \frac{\varepsilon - \mu}{T_e}, \quad (31)$$

$$\sigma_{\text{E}h\text{A}}^{T_e} = \frac{\tau_p}{4\pi\hbar}g(\mu - 1.5k_{\text{B}}T_e) \int_{\frac{\Delta_{\text{SAS}}}{2}}^{\infty} d\varepsilon \theta(-\varepsilon + \mu) \left(-\frac{\partial f^{(0)}}{\partial \varepsilon} \right) \frac{\varepsilon - \mu}{T_e}. \quad (32)$$

Similarly approximate expressions, $L_{\text{E}e\text{A}}^{T_e}$ and $L_{\text{E}h\text{A}}^{T_e}$, are obtained. Figure 5(a) and (b) show that thus obtained approximate estimates $\sigma_{\text{E}A}^{T_e} = \sigma_{\text{E}e\text{A}}^{T_e} + \sigma_{\text{E}h\text{A}}^{T_e}$ and $L_{\text{E}A}^{T_e} = L_{\text{E}e\text{A}}^{T_e} + L_{\text{E}h\text{A}}^{T_e}$ (red lines) well reproduce $\sigma_{\text{E}}^{T_e}$ and $L_{\text{E}}^{T_e}$ (black lines). Since the peak in each of $\sigma_{\text{E}}^{T_e}$ and $L_{\text{E}}^{T_e}$ is located around $\mu = \Delta_{\text{SAS}}/2 + 1.5k_{\text{B}}T_e$, we estimate the peak height at $\mu = \Delta_{\text{SAS}}/2 + 1.5k_{\text{B}}T_e$ where the hole contribution $\sigma_{\text{E}h\text{A}}^{T_e} = L_{\text{E}h\text{A}}^{T_e} = 0$. Then estimated peak values $\sigma_{\text{E}A}^{T_e\mathcal{P}}$ and $L_{\text{E}A}^{T_e\mathcal{P}}$ become

$$\sigma_{\text{E}A}^{T_e\mathcal{P}} = \frac{\tau_p k_{\text{B}} \ln 2}{4\pi\hbar} g \left(\frac{\Delta_{\text{SAS}}}{2} + 3k_{\text{B}}T_e \right), \quad (33)$$

$$L_{\text{E}A}^{T_e\mathcal{P}} = \frac{e\tau_p k_{\text{B}} \ln 2}{2\pi\hbar} h \left(\frac{\Delta_{\text{SAS}}}{2} + 3k_{\text{B}}T_e \right). \quad (34)$$

Both $\sigma_{\text{E}A}^{T_e\mathcal{P}}$ and $L_{\text{E}A}^{T_e\mathcal{P}}$ increase by switching on the interwell coupling, that is $\frac{d}{d\Delta_{\text{SAS}}}\sigma_{\text{E}A}^{T_e\mathcal{P}} > 0$ and $\frac{d}{d\Delta_{\text{SAS}}}L_{\text{E}A}^{T_e\mathcal{P}} > 0$ at $\Delta_{\text{SAS}} = 0$, which are derived from $\frac{d}{d\Delta_{\text{SAS}}}k > 0$, $\frac{d}{d\Delta_{\text{SAS}}}\Delta_k = 0$, and $\frac{d}{d\Delta_{\text{SAS}}}v_{\text{E}k} > 0$ at $\Delta_{\text{SAS}} = 0$. Here k is determined by $\varepsilon_{\text{E}k} = \Delta_{\text{SAS}}/2 + 3k_{\text{B}}T_e$ and then depends on Δ_{SAS} . Therefore enhancements of the momentum (k) and the velocity ($v_{\text{E}k}$) by Δ_{SAS} at $\Delta_{\text{SAS}} = 0$ lead to those of $\sigma_{\text{E}A}^{T_e\mathcal{P}}$ and $L_{\text{E}A}^{T_e\mathcal{P}}$, which can explain the reason why the l -TISP exhibits its maximum at a non-zero Δ_{SAS} in Figure 3.

B. Spin Current

In this section we show that the spin current into the adjacent electrode is proportional to the l -TISP as derived for the spin current extracted from the local CISP [37] in a simplified model of the electron tunneling to the electrode. The spin current per unit area, $j_{z,\xi}^s$, from the DQWS to electrode ξ is given by

$$j_{z,\xi}^s = \frac{1}{S} \sum_{\sigma_y} \frac{\hbar \sigma_y}{2} \sum_{n\sigma\mathbf{k}} \sum_{k_z} W_{\xi\mathbf{k}k_z\sigma_y, n\sigma\mathbf{k}} [f_{n\mathbf{k}} - f^{(0)}(\varepsilon_{\mathbf{k}k_z}, \mu^{\text{eq}}, T_e^{\text{eq}})], \quad (35)$$

where we assumed that each electrode is in equilibrium with the chemical potential μ^{eq} and the temperature T_e^{eq} , which are spatially uniform in contrast to spatially-varying $\mu(\mathbf{r})$ and $T_e(\mathbf{r})$ in $f^{(0)}$ [Equation (14)] of the DQWS. The tunneling rate between DQWS and electrode ξ is given by

$$W_{\xi\mathbf{k}k_z\sigma_y, n\sigma\mathbf{k}} = \frac{2\pi}{\hbar} |\langle \xi\mathbf{k}k_z\sigma_y | H_{\text{T}} | n\sigma\mathbf{k} \rangle|^2 \delta(\varepsilon_{n\mathbf{k}} - \varepsilon_{\mathbf{k}k_z}). \quad (36)$$

We assume that the tunneling occurs between the well and the electrode in the same side without changing the inplane momentum \mathbf{k} and the spin. Then the tunneling Hamiltonian H_{T} is given by

$$H_{\text{T}} = \sum_{\xi\mathbf{k}k_z\sigma_y} |\xi\mathbf{k}\sigma_y\rangle \langle \xi\mathbf{k}\sigma_y | H_{\text{T}} | \xi\mathbf{k}k_z\sigma_y\rangle \langle \xi\mathbf{k}k_z\sigma_y | + \text{h.c.}, \quad (37)$$

where $|\xi\mathbf{k}\sigma_y\rangle = |\xi\rangle|\mathbf{k}\rangle|\sigma_y\rangle$ is the wave function localized in well ξ and h.c. denotes the Hermitian conjugate of the preceding term. We additionally assume that the matrix element $\langle \xi\mathbf{k}\sigma_y | H_{\text{T}} | \xi\mathbf{k}k_z\sigma_y\rangle$ has no dependence on \mathbf{k} , σ_y , and ξ . The distribution difference in Equation (35) is divided into $f_{n\mathbf{k}} - f^{(0)}(\varepsilon_{n\mathbf{k}}, \mu(\mathbf{r}), T_e(\mathbf{r})) = f_{n\mathbf{k}}^{(1)}$ and $f^{(0)}(\varepsilon_{n\mathbf{k}}, \mu(\mathbf{r}), T_e(\mathbf{r})) - f^{(0)}(\varepsilon_{\mathbf{k}k_z}, \mu^{\text{eq}}, T_e^{\text{eq}})$. The latter produces no spin current because it is isotropic in \mathbf{k} space and the former $f_{n\mathbf{k}}^{(1)}$ gives

$$j_{z,\xi}^s = \frac{\hbar}{2S} \sum_{n\sigma\mathbf{k}} \frac{1}{\tau_{\xi}} f_{n\mathbf{k}}^{(1)} \langle n\sigma\mathbf{k} | \hat{\sigma}_y P_{\xi} | n\sigma\mathbf{k} \rangle \quad (38)$$

where τ_{ξ} is the lifetime of state $|\xi\mathbf{k}\sigma_y\rangle$ due to tunneling into electrode ξ , defined by

$$\frac{1}{\tau_{\xi}} = \sum_{k_z} \frac{2\pi}{\hbar} |\langle \xi\mathbf{k}\sigma_y | H_{\text{T}} | \xi\mathbf{k}k_z\sigma_y\rangle|^2 \delta(\varepsilon_{n\mathbf{k}} - \varepsilon_{\mathbf{k}k_z}). \quad (39)$$

We neglect the variation of $\langle \xi \mathbf{k} \sigma_y | H_T | \xi \mathbf{k} k_z \sigma_y \rangle$ with k_z by choosing a sufficiently large value of $|\varepsilon_0|$ such that $|\varepsilon_0| \gg \varepsilon_{F0}$ [37]. Then the spin current is shown to be proportional to the l -TISP $\sigma_{y\xi}$:

$$j_{z,\xi}^s = \frac{1}{\tau_\xi} \frac{\hbar}{2} \sigma_{y\xi}. \quad (40)$$

V. CONCLUSIONS

We have considered the double-quantum-well structure (DQWS) as the simplest system with locally-broken inversion symmetry and theoretically studied thermally-induced local spin polarization (l -TISP) which can be extracted as spin current. We have calculated the l -TISP using the Boltzmann equation in the relaxation-time approximation under the condition of zero charge current with an aim to search optimum strengths of the Rashba SOI and the interwell coupling which maximize the magnitude of the l -TISP. We have found that the l -TISP exhibits the maximum at a finite Rashba SOI and a nonzero interwell coupling when the electron density is fixed. The finite optimum value of the Rashba-SOI stems from the fact that the optimum position of the chemical potential to maximize the l -TISP is near the first-excited subband bottom where the thermal current transfers electrons from the ground subband with negative local spin polarization to the first-excited subband with positive local spin polarization, leading to the largest induced spin polarization. We have also presented a possible explanation for the nonzero optimum value of the interwell coupling: the interwell coupling increases magnitudes of the momentum and the group velocity at the most probable energy in the first-excited subband and consequently enhances the l -TISP. We have derived the formula for the spin current into an electrode, which is generated from the antiparallel TISP with a selective coupling of the electrode to one well of the DQWS, and shown that it is proportional to the l -TISP in the well by assuming the same tunneling rate to the electrode for all occupied eigenstates in the DQWS.

We have also confirmed, from Figure 3 (a) and (b) (along $\Delta_{SAS} = 0$ line), that the largest TISP in a decoupled well, that is the 2DES, appears at the chemical potential near the bottom of the first-excited subband at $\mathbf{k} = 0$ where the ground and first-excited subbands have the

same energy in the 2DES. The TISP of the 2DES with the Rashba SOI was already calculated in several previous studies [15–19]. Some of them [16, 18, 19] calculated the TISP without imposing the condition of zero charge current, that is in the absence of the electrochemical-potential gradient and showed [16, 19] that the largest absolute value of the TISP appears near the ground subband bottom (which is at nonzero \mathbf{k} in the 2DES). In this paper we have found, in the standard experimental condition with zero charge current, that the higher peak appears near the first-excited subband bottom because the peak in the ground subband is suppressed by the opposite contribution from the electrochemical-potential gradient. Other calculations [15, 17] of the TISP in the 2DES were made under the condition of zero charge current. These calculations focused on the region of the Fermi energy much larger than $k_B T_e$ which is away from the first-excited subband bottom where we have found the maximum of the TISP.

In this paper we have revealed that the l -TISP (the TISP) is the largest at the chemical potential near the bottom of the first-excited subband in the DQWS (2DES) and that the coupling between wells in the DQWS enhances the l -TISP. These findings will be useful in designing the optimum TISP device.

ACKNOWLEDGMENT

This work was partly supported by Grant-in-Aid for Scientific Research (C) Grant No. JP21K03413 from the Japan Society for the Promotion of Science (JSPS).

-
- [1] V. Edelstein, Spin polarization of conduction electrons induced by electric current in two-dimensional asymmetric electron systems, *Solid State Commun.* **73**, 233 (1990).
 - [2] V. K. Kalevich and V. L. Korenev, Effect of electric field on the optical orientation of 2D electrons, *JETP Lett.* **52**, 230 (1990).
 - [3] A. Y. Silov, P. A. Blajnov, J. H. Wolter, R. Hey, K. H. Ploog, and N. S. Averkiev, Current-induced spin polarization at a single heterojunction, *Appl. Phys. Lett.* **85**, 5929 (2004).

- [4] Y. K. Kato, R. C. Myers, A. C. Gossard, and D. D. Awschalom, Current-induced spin polarization in strained semiconductors, *Phys. Rev. Lett.* **93**, 176601 (2004).
- [5] C. L. Yang, H. T. He, L. Ding, L. J. Cui, Y. P. Zeng, J. N. Wang, and W. K. Ge, Spectral dependence of spin photocurrent and current-induced spin polarization in an InGaAs/InAlAs two-dimensional electron gas, *Phys. Rev. Lett.* **96**, 186605 (2006).
- [6] M. Trushin and J. Schliemann, Anisotropic current-induced spin accumulation in the two-dimensional electron gas with spin-orbit coupling, *Phys. Rev. B* **75**, 155323 (2007).
- [7] A. R. Mellnik, J. S. Lee, A. Richardella, J. L. Grab, P. J. Mintun, M. H. Fischer, A. Vaezi, A. Manchon, E.-A. Kim, N. Samarth, and D. C. Ralph, Spin-transfer torque generated by a topological insulator, *Nature* **511**, 449 (2014).
- [8] K. Kondou, R. Yoshimi, A. Tsukazaki, Y. Fukuma, J. Matsuno, K. S. Takahashi, M. Kawasaki, Y. Tokura, and Y. Otani, Fermi-level-dependent charge-to-spin current conversion by Dirac surface states of topological insulators, *Nat. Phys.* **12**, 1027 (2016).
- [9] K. Kondou, H. Tsai, H. Isshiki, and Y. Otani, Efficient spin current generation and suppression of magnetic damping due to fast spin ejection from nonmagnetic metal/indium-tin-oxide interfaces, *APL Materials* **6**, 101105 (2018), <https://doi.org/10.1063/1.5050848>.
- [10] M. B. Jungfleisch, W. Zhang, J. Sklenar, W. Jiang, J. E. Pearson, J. B. Ketterson, and A. Hoffmann, Interface-driven spin-torque ferromagnetic resonance by Rashba coupling at the interface between nonmagnetic materials, *Phys. Rev. B* **93**, 224419 (2016).
- [11] Q. Shao, G. Yu, Y.-W. Lan, Y. Shi, M.-Y. Li, C. Zheng, X. Zhu, L.-J. Li, P. K. Amiri, and K. L. Wang, Strong rashba-edelstein effect-induced spin-orbit torques in monolayer transition metal dichalcogenide/ferromagnet bilayers, *Nano Letters* **16**, 7514 (2016).
- [12] Y. Wang, R. Ramaswamy, M. Motapothula, K. Narayanapillai, D. Zhu, J. Yu, T. Venkatesan, and H. Yang, Room-temperature giant charge-to-spin conversion at the SrTiO₃-LaAlO₃ oxide interface, *Nano Letters* **17**, 7659 (2017).
- [13] Y. Liu and Q. Shao, Two-dimensional materials for energy-efficient spin-orbit torque devices, *ACS Nano* **14**, 9389 (2020).
- [14] S. Karube, N. Tezuka, M. Kohda, and J. Nitta, Anomalous spin-orbit field via the rashba-edelstein effect at the W/Pt interface, *Phys. Rev. Applied* **13**, 024009 (2020).

- [15] C. Wang and M. Pang, Thermally induced spin polarization and thermal conductivities in a spin-orbit-coupled two-dimensional electron gas, *Solid State Communications* **150**, 1509 (2010).
- [16] A. Dyrdał, M. Inglot, V. K. Dugaev, and J. Barnaś, Thermally induced spin polarization of a two-dimensional electron gas, *Phys. Rev. B* **87**, 245309 (2013).
- [17] S. Tölle, C. Gorini, and U. Eckern, Room-temperature spin thermoelectrics in metallic films, *Phys. Rev. B* **90**, 235117 (2014).
- [18] C. Xiao, D. Li, and Z. Ma, Thermoelectric response of spin polarization in rashba spintronic systems, *Frontiers of Physics* **11**, 117201 (2016).
- [19] A. Dyrdał, J. Barnaś, V. K. Dugaev, and J. Berakdar, Thermally induced spin polarization in a magnetized two-dimensional electron gas with rashba spin-orbit interaction, *Phys. Rev. B* **98**, 075307 (2018).
- [20] F. J. Ohkawa and Y. Uemura, Quantized surface states of a narrow-gap semiconductor, *J. Phys. Soc. Jpn.* **37**, 1325 (1974).
- [21] Y. A. Bychkov and E. I. Rashba, Oscillatory effects and the magnetic susceptibility of carriers in inversion layers, *J. Phys. C* **17**, 6039 (1984).
- [22] Y. A. Bychkov and E. I. Rashba, Properties of a 2D electron gas with lifted spectral degeneracy, *JETP Lett.* **39**, 78 (1984).
- [23] S. Faniel, T. Matsuura, S. Mineshige, Y. Sekine, and T. Koga, Determination of spin-orbit coefficients in semiconductor quantum wells, *Phys. Rev. B* **83**, 115309 (2011).
- [24] Y. Yanase, Magneto-electric effect in three-dimensional coupled zigzag chains, *Journal of the Physical Society of Japan* **83**, 014703 (2014).
- [25] X. Zhang, Q. Liu, J.-W. Luo, A. J. Freeman, and A. Zunger, Hidden spin polarization in inversion-symmetric bulk crystals, *Nat. Phys.* **10**, 387 (2014).
- [26] J. Železný, H. Gao, K. Výborný, J. Zemen, J. Mašek, A. Manchon, J. Wunderlich, J. Sinova, and T. Jungwirth, Relativistic néel-order fields induced by electrical current in antiferromagnets, *Phys. Rev. Lett.* **113**, 157201 (2014).
- [27] J. M. Riley, F. Mazzola, M. Dendzik, M. Michiardi, T. Takayama, L. Bawden, C. Granerød, M. Leandersson, T. Balasubramanian, M. Hoesch, T. K. Kim, H. Takagi, W. Meevasana, P. Hofmann, M. S. Bahramy, J. W. Wells, and P. D. C. King, Direct observation of spin-

- polarized bulk bands in an inversion-symmetric semiconductor, *Nat. Phys.* **10**, 835 (2014).
- [28] P. Wadley, B. Howells, J. Železný, C. Andrews, V. Hills, R. P. Campion, V. Novák, K. Olejník, F. Maccherozzi, S. S. Dhesi, S. Y. Martin, T. Wagner, J. Wunderlich, F. Freimuth, Y. Mokrousov, J. Kuneš, J. S. Chauhan, M. J. Grzybowski, A. W. Rushforth, K. W. Edmonds, B. L. Gallagher, and T. Jungwirth, Electrical switching of an antiferromagnet, *Science* **351**, 587 (2016).
- [29] M. Gehlmann, I. Aguilera, G. Bihlmayer, E. Mlynczak, M. Eschbach, S. Döring, P. Gospodaric, S. Cramm, B. Kardynal, L. Plucinski, S. Blügel, and C. M. Schneider, Quasi 2D electronic states with high spin-polarization in centrosymmetric mos2 bulk crystals, *Sci. Rep.* **6**, 26197 (2016).
- [30] D. Santos-Cottin, M. Casula, G. Lantz, Y. Klein, L. Petaccia, P. Le Fèvre, F. Bertran, E. Pappalazarou, M. Marsi, and A. Gauzzi, Rashba coupling amplification by a staggered crystal field, *Nat. Commun.* **7**, 11258 (2016).
- [31] S.-L. Wu, K. Sumida, K. Miyamoto, K. Taguchi, T. Yoshikawa, A. Kimura, Y. Ueda, M. Arita, M. Nagao, S. Watauchi, I. Tanaka, and T. Okuda, Direct evidence of hidden local spin polarization in a centrosymmetric superconductor $\text{LaO}_{0.55}\text{F}_{0.45}\text{BiS}_2$, *Nat. Commun.* **8**, 1919 (2017).
- [32] W. Yao, E. Wang, H. Huang, K. Deng, M. Yan, K. Zhang, K. Miyamoto, T. Okuda, L. Li, Y. Wang, H. Gao, C. Liu, W. Duan, and S. Zhou, Direct observation of spin-layer locking by local Rashba effect in monolayer semiconducting ptse2 film, *Nat. Commun.* **8**, 14216 (2017).
- [33] E. Razzoli, T. Jaouen, M.-L. Mottas, B. Hildebrand, G. Monney, A. Pisoni, S. Muff, M. Fanciulli, N. C. Plumb, V. A. Rogalev, V. N. Strocov, J. Mesot, M. Shi, J. H. Dil, H. Beck, and P. Aebi, Selective probing of hidden spin-polarized states in inversion-symmetric bulk mos₂, *Phys. Rev. Lett.* **118**, 086402 (2017).
- [34] H. Watanabe and Y. Yanase, Symmetry analysis of current-induced switching of antiferromagnets, *Phys. Rev. B* **98**, 220412 (2018).
- [35] C. Cheng, J.-T. Sun, X.-R. Chen, and S. Meng, Hidden spin polarization in the 1t-phase layered transition-metal dichalcogenides MX_2 (M=Zr, Hf; X=S, Se, te), *Sci. Bull.* **63**, 85 (2018).
- [36] L. Yuan, Q. Liu, X. Zhang, J.-W. Luo, S.-S. Li, and A. Zunger, Uncovering and tailoring hidden Rashba spin-orbit splitting in centrosymmetric crystals, *Nat. Commun.* **10**, 906 (2019).

- [37] Y. Suzuki, Y. Kitagawa, S.-i. Tezuka, and H. Akera, Spin-current generation from local spin polarization induced by current through local inversion asymmetry: Double quantum well structure, *Phys. Rev. B* **107**, 115306 (2023).
- [38] Y. Kitagawa, Y. Suzuki, S.-i. Tezuka, and H. Akera, Spin current between buckled atomic layers with a twist generated by locally broken inversion symmetry, *Phys. Rev. B* **108**, 115431 (2023).
- [39] T. Kato and H. Akera, Antiparallel spin polarization induced by current in a bilayer, *physica status solidi (b)* **n/a**, 2300237 (2023).
- [40] T. Jungwirth, X. Marti, P. Wadley, and J. Wunderlich, Antiferromagnetic spintronics, *Nat. Nanotechnol.* **11**, 231 (2016).
- [41] T. Koga, J. Nitta, H. Takayanagi, and S. Datta, Spin-filter device based on the Rashba effect using a nonmagnetic resonant tunneling diode, *Phys. Rev. Lett.* **88**, 126601 (2002).
- [42] P.-Q. Jin and Y.-Q. Li, Magnification of the spin Hall effect in a bilayer electron gas, *Phys. Rev. B* **76**, 235311 (2007).
- [43] E. Bernardes, J. Schliemann, M. Lee, J. C. Egues, and D. Loss, Spin-orbit interaction in symmetric wells with two subbands, *Phys. Rev. Lett.* **99**, 076603 (2007).
- [44] R. S. Calsaverini, E. Bernardes, J. C. Egues, and D. Loss, Intersubband-induced spin-orbit interaction in quantum wells, *Phys. Rev. B* **78**, 155313 (2008).
- [45] M. Akabori, S. Hidaka, H. Iwase, S. Yamada, and U. Ekenberg, Realization of $\text{In}_{0.75}\text{Ga}_{0.25}\text{As}$ two-dimensional electron gas bilayer system for spintronics devices based on Rashba spin-orbit interaction, *J. Appl. Phys.* **112**, 113711 (2012).
- [46] F. G. G. Hernandez, L. M. Nunes, G. M. Gusev, and A. K. Bakarov, Observation of the intrinsic spin Hall effect in a two-dimensional electron gas, *Phys. Rev. B* **88**, 161305 (2013).
- [47] S. Souma, A. Sawada, H. Chen, Y. Sekine, M. Eto, and T. Koga, Spin blocker using the interband Rashba effect in symmetric double quantum wells, *Phys. Rev. Applied* **4**, 034010 (2015).
- [48] A. Khaetskii and J. C. Egues, Giant edge spin accumulation in a symmetric quantum well with two subbands, *EPL* **118**, 57006 (2017).

- [49] K. Hayashida and H. Akera, D'yakonov-perel' spin relaxation in a bilayer with local structural inversion asymmetry, *Phys. Rev. B* **101**, 035306 (2020).
- [50] N. W. Ashcroft and N. D. Mermin, Solid State Physics (Saunders College, Philadelphia, 1976).
- [51] T. Ishikawa and H. Akera, Antiparallel spin Hall current in a bilayer with skew scattering, *Phys. Rev. B* **100**, 125307 (2019).
- [52] T. Ishikawa and H. Akera, Ac response of spin-pseudospin current in a double quantum well, *Jpn. J. Appl. Phys.* **61**, 063002 (2022).